Multi-period operation of integrated electricity and gas systems with hydrogen blending considering gas composition dynamics

Sheng Wang [a,b,c], Hongxun Hui [a,b,*], Tao Chen [d], Junyi Zhai [e]

[a] *State Key Laboratory of Internet of Things for Smart City, University of Macau, 999078, Macao Special Administrative Region of China*
[b] *Department of Electrical and Computer Engineering, University of Macau, 999078, Macao Special Administrative Region of China*
[c] *School of Engineering, Newcastle University, Newcastle-upon-Tyne, NE1 7RU, UK*
[d] *Department of Electrical Engineering, Southeast University, NanJing, 210000, China*
[e] *College of New Energy, China University of Petroleum (East China), Qingdao, 266580, China*

ARTICLE INFO

ABSTRACT

Green hydrogen from renewable sources can be blended with natural gas and serves as a potentially feasible measure for contributing to the net zero energy sector. The time-varying nature of hydrogen injection, influenced by stochastic renewable generations, can result in fluctuations in gas concentrations in the entire network. It poses a potential threat to the secure regulation of integrated electricity and gas systems (IEGS). For managing the operating condition and guaranteeing the security of IEGS during operation, a multi-period operation framework with alternative gas (e.g., hydrogen) blending is developed. First, a convex gas security range is derived using the Dutton method. Then, the multi-period operation framework is devised to mitigate the impacts of alternative gas injection on gas security over the entire operational period. Both the dynamics from gas composition and gas flow are modelled, accurately describing the real-time travel of alternative gas concentrations. The dynamics in the gas mixture properties (e.g., relative density) are fully revealed with time-varying gas concentrations. To tackle the high non-convexities in the optimization problem, second-order-cone relaxation is well-tailored and firstly used in the case of varying gas compositions, making the motion equations and advective transport equations more tractable. An advanced second-order-cone sequential programming is devised to drive the relaxation tight more efficiently. Finally, our operation strategy is illustrated in IEEE and Belgium Electricity and Gas Systems. Results indicate that hydrogen concentrations take about 12.5 h to travel from the injection point to the end of the pipeline route in the Belgium gas system. By incorporating this unique characteristic into the model, operational scheduling and dispatch in IEGS can be more practical when integrating hydrogen in the future.

1. Introduction

Alternative gases, e.g., green hydrogen, produced from power-to-gas (PTG) facilities using surplus renewable energy, present a promising solution for low-carbon energy systems. Blending these gases with natural gas in pipelines offers a means to transport them to meet diverse energy demands [1,2]. Many countries have started their early trials for alternative gas blending projects. The UK's "HyDeploy" project, launched in 2017, successfully supplied hydrogen-mixed gas to over 100 homes and 30 university buildings [3]. In 2019, China's first commercial demonstration project on hydrogen blending in Chaoyang safely ran for one year with 10% hydrogen concentration [4]. Owing to the considerable proportion of natural gas in the power generation structure and increased PTG capacity, the interdependence between electricity and gas has led to the conceptualization of integrated electricity and gas systems (IEGS) [5].

However, stochastic renewable energy generation introduces variability in alternative gas injection, causing fluctuations in gas compositions across the network. This poses great challenges to the secure operation of IEGS. High hydrogen concentration alters the gross calorific value of the gas mixture, impacting heat energy produced during combustion, and potentially shortening the lifespan of gas appliances [6]. Additionally, varying hydrogen concentrations influence physical properties such as relative density, leading to gas flow variations and potential linepack swings that increase the complexity of gas system operation [7]. Therefore, ensuring gas composition remains within a secure range is crucial for the safe operation of IEGS under uncertain and distributed hydrogen injections.

---

* Corresponding author.
E-mail address: hongxunhui@um.edu.mo (H. Hui).

So far, most previous research efforts are dedicated to tracking the gas concentrations across the gas system with alternative gas injections. For example, the steady-state simulation is carried out in [8] for calculating the distribution of gas composition. The gas flow model is formulated using algebraic equations and is solved by the Newton–Raphson method. The IEGS and hydrogen blending are used to absorb solar generations and their hydrogen production in [9]. Different scenarios are formed for uncertain solar installations, and the electrical and gas networks are simulated sequentially to assess the impact of hydrogen injections in different locations, while keeping the gas composition in a secured range. The probabilistic multi-energy flow model, including electricity and hydrogen-blended natural gas, is established in [10] considering multiple uncertainties. Jacobian matrix is formulated for the steady-state multi-energy flow model, and the cumulant method and Nataf transformation are applied to calculate the energy flow considering the uncertainty correlations. The simulation model for hydrogen blended IEGS is further refined in [11], where the compressibility factor of gas and friction factor of pipelines are formulated in nonlinear form for better accuracy, but the simulation also becomes more computationally burdensome. Using these simulation models, [12] studies the impacts of different injection locations and modes. It concludes that blending hydrogen in the upper pipeline is better than downstream pipelines, and the concentrated hydrogen blending strategy is better than the dispersed one. The reliability of hydrogen blended IEGS is studied in [13]. Though the optimization model is formulated, the hydrogen blending ratio is assumed to be constant, which cannot be adjusted with renewable generations or according to gas security. Despite that these studies significantly contribute to the basic steady-state gas flow modelling with variant gas composition, they only solve algebra equations to simulate the impact of hydrogen injection. In other words, they often lack active and quantitative measures for maintaining system security in the face of violations of physical conditions or gas security.

Recently, some optimization-oriented studies have emerged and try to address this gap by investigating optimal operation strategies for IEGS with varying gas compositions. These studies with active decision-making can help the system operator to improve the cost-benefits and securities under alternative gas injections. A coordinated optimal operation framework of IEGS considering gas composition tracking is firstly developed in [14]. Inevitably it faces the challenge of nonlinearities due to the introduction of variant gas composition. A general nonlinear solver is used for the solution, but the computation efficiency and credibility cannot be guaranteed. Moreover, the optimal energy flow of power and gas systems is implemented separately, so the global optimality can be undermined. A distributionally robust optimization framework is introduced in this problem to handle the wind uncertainties in [15], but the nonlinear impacts of varying gas composition on gas physical properties are neglected. To tackle the nonlinearity and nonconvextity problem in the steady-state hydrogen-gas optimization, advanced sequential programming is introduced in [16]. The nonlinear gas security indices, such as the Wobbe index, are also linearized as well. However, the gas flow direction is usually prespecified to avoid introducing integer variables. A mixed integer linear programming optimization framework is proposed in [17] to explore the additional flexibility of the gas system during power system scheduling. A unified modelling approach for gas flow dynamics is proposed in [18] and demonstrates that it can use linepack more accurately than relaxation-based approaches. Different solution approaches, including polyhedral envelope, piecewise linearization, and iterative-based methods for solving multi-period gas system operation problems are compared in [19]. The steady-state, quasi-dynamic, and full dynamic models and solution methods are fully reviewed in [20], which build a comprehensive knowledge base for modelling our gas flow dynamics with varying gas compositions. The flexibility provided by linepack, with hydrogen injections, is quantified in [21]. Based on these models, the impacts of

short-term and long-term reliabilities, and resilience, are quantitatively explored in [22–24], respectively.

A common drawback of the aforementioned studies is that their optimization models are formulated on a steady-state basis, while overlooking the dynamics inherent in gas systems. The intermittency of renewable generations introduces fluctuations in hydrogen injections and gas compositions during operation. Since the gas dynamics are far slower than the electricity system, it will be inaccurate to ignore the gas dynamics if the optimization model is applied to the operational horizon. There are two types of dynamics in gas systems. The first is the gas flow dynamics, which can serve as a flexible resource in IEGS operation and scheduling scenarios [25,26]. The second type, gas composition dynamics, stands out as unique to gas systems featuring varying gas compositions. It describes how a certain gas content travels across the gas network. For instance, if hydrogen is injected at the inlet of a pipeline, it will take some time to be gradually transported to the outlet, resulting in a period during which the gas concentration at the outlet remains unchanged.

It is pivotal to understand these two dynamic features in the optimal operation of IEGS, especially in scenarios involving alternative gas injections. Although the modelling of gas flow dynamics has been well incorporated into the power system operation using finite difference schemes [26,27], finite volume schemes [28,29], and analytical methods [30,31], these methods can only be applied when the gas composition is constant. The temporal and spatial evolution of gas composition must be considered to accurately capture the system's response to changes introduced at various points within the network. Gas composition dynamics can be mathematically modelled by a group of nonlinear partial derivative equations (PDEs). Incorporating these terms will make the optimization model non-convex and time-interdependent. It not only increases the computation burden dramatically, but also makes the problem intractable. Moreover, the travel of gas composition brings inconsistency to the relative density, heat value, etc. of the gas mixture, which also brings high nonconvexities to the gas flow equations as well. Due to the above reasons, though the gas composition dynamics have been studied in traditional gas network simulations [32–34], it has seldom been incorporated in the coordinated optimal operation of IEGS. The coordinated operation model and solution of electricity and hydrogen-gas system is introduced in [35], but the linear approximation is used for convexification.

In summary, the optimization of IEGS operation with variant hydrogen injection is still at the early stage, especially with the presence of both gas flow and gas composition dynamics. The multi-period optimization framework for this problem is unclear, and there is merely a tractable and highly efficient solution method to this optimization problem due to the large-scale variables, time-interdependency, and various forms of nonlinearities and noncovexities both in the physical laws and gas security regulations. To address these research gaps, this paper develops the multi-period coordinated operation scheme in IEGS with the blending of various alternative gases, specifically considering dynamics in the gas concentration. The key contributions of this work are:

(i) A multi-period optimal energy flow (MPOEF) scheme of IEGS with hydrogen blending considering the gas composition dynamics is proposed. Compared with the previous optimal energy flow models in IEGS considering gas flow dynamics [27,30,31], our proposed model can be applied to variant gas composition scenarios. Compared with previous steady-state gas composition tracking models (e.g., [14,15], etc.): (1) This model accurately characterizes the real-time travel of alternative gas concentrations across the gas network, modelling both gas flow and gas composition dynamics. (2) It introduces variables to represent the dynamics in physical properties, comprehensively revealing and controlling the impacts of hydrogen at the nodal scale.
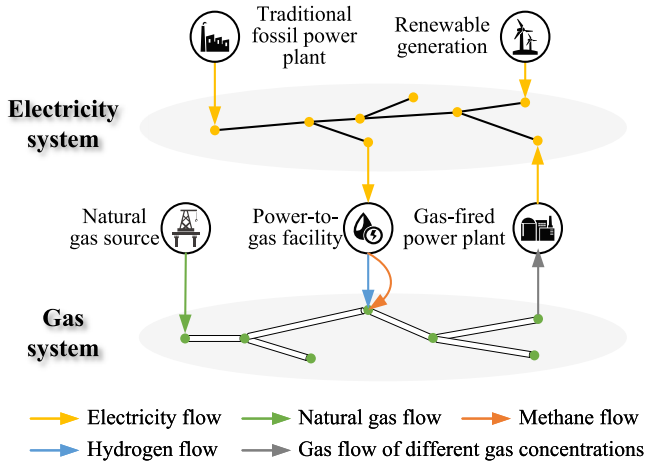
Fig. 1. Schematic diagram of integrated electricity and gas systems with hydrogen blending.

(3) The concept of linepack energy is introduced to set terminal conditions, enhancing gas system flexibility against fluctuating hydrogen injections while maintaining end-of-operation robustness.

(ii) The convex gas security range is proposed based on various indices (such as the Wobbe index (WI)). Compared with the traditional Dutton method [36], it can (1) guarantee the convexity of the MPOEF problem by linearizing the security constraints; (2) better control the combustion security of the IEGS in the hydrogen blending scenario by introducing the new flame speed (FS) index.

(iii) A tractable solution method for the highly non-convex MPOEF problem is proposed. To the best of our knowledge, the second-order cone (SOC) reformulation is tailored for the first time in this paper to convexify the discretized motion and advective transport PDEs in the presence of varying gas compositions. It can fully utilize the second-order information of these constraints to improve computation efficiency. Advanced sequential SOC programming with adaptive penalty factors also ensures convergence and optimality.

2. Convex gas security range

The structure of the IEGS with hydrogen blending is illustrated in Fig. 1. Comprising two layers, the electricity system includes conventional fossil units (using non-gas fuels to generate electricity), renewable generators, and gas-fired power plants (GPP) to generate electricity. The gas system relies on gas sources and power-to-gas (PTG) facilities for natural gas, hydrogen, and methane. These gases will be mixed at hydrogen injection points, and then transported to meet diverse gas demands.

To guarantee the security of gas system components, gas security requirements must be adhered to. Gas compositions may vary across the network due to different gas sources and PTGs. The Dutton method is employed to define a convex gas security range, widely used in regions such as the UK and Australia, as depicted in Fig. 2 [37]. Gas security is constrained by indices including the WI, incomplete combustion factor (ICF), and soot index (SI) [38]. The Dutton method, however, becomes nonconvex when projected onto the plane formed by the concentrations of different gas components, which may cause the following optimization problem intractable, as depicted in Fig. 2. To address this, we formulate a convex gas security range by linearizing gas security indices, as in ((1)–(4)).

The flame speed factor describes the approximate maximum velocity with which a flame can travel in any gas-air mixture. Hydrogen has

about seven times higher flame speed than natural gas. This means, when hydrogen is ignited, the front of the flame may travel back reversely, causing severe safety problems [39]. Therefore, it is crucial to control the hydrogen fraction in the natural gas to restrain the flame speed within an acceptable range. FS is additionally introduced to the Dutton method here. An assumption (which has been validated by practice) is made that, the maximum flame velocity of a gas mixture can be regarded as a linear function of each gas component. This leads to the flame speed calculation formulation in (4) [40]:

$$\mathbb{H} = \left\{ \boldsymbol{\phi}_{i,k} \mid WI^{min} \leq WI_{i,k}; ICF_{i,k} \leq ICF^{max}; SI_{i,k} \leq SI^{max}; \atop FS_{i,k} \leq FS_{i,k}^{max}; \mathbf{0} \leq \boldsymbol{\phi}_{i,k} \leq \mathbf{1}; \right\}, \forall i \in \mathcal{I}, \forall k \in \mathcal{K} \quad (1)$$

$$WI_{i,k} = HV_{i,k} / \left((S^{ng})^{\frac{1}{2}} + (S^{ng})^{-\frac{1}{2}} S_{i,k} \right) \quad (2)$$

$$ICF_{i,k} = (WI_{i,k} - 50.73 + 0.03\phi_{i,k}^{np})/1.56 - 0.01\phi_{i,k}^{hy} \quad (3)$$

$$SI_i = 0.896 tan^{-1}(0.0255\phi_{i,k}^{pr} - 0.0233\phi_{i,k}^{ni} - 0.0091\phi_{i,k}^{hy} + 0.617)$$

$$FS_{i,k} = \sum_{n \in \mathcal{N}} \phi_{i,k,n} f s_n \quad (4)$$

where $\mathbb{H}$ is the gas security range in the normal condition; $\boldsymbol{\phi}_{i,k}$ is the set of gas compositions at node i at time k; $\phi_{i,k}^{hy}$, $\phi_{i,k}^{pr}$, and $\phi_{i,k}^{ni}$ are the concentrations of hydrogen, propane, and nitrogen, respectively; $WI_{i,k}$, $ICF_{i,k}$, $SI_{i,k}$, $FS_{i,k}$, $HV_{i,k}$, and $S_{i,k}$ are the WI, ICF, SI, FS, heat value, and relative density of the gas mixture at node i in time k, respectively; S^{ng} is the relative density of natural gas; WI^{min} is the minimum value of WI; ICF^{max}, SI^{max}, and FS^{max} are the maximum values of ICF, SI, and FS, respectively; $\mathcal{I}$ and $\mathcal{K}$ are the sets of nodes and times, respectively; fs_n is the flame speed of gas component n in the fuel–air mixture.

The nodal heat value and relative density depend on the nodal gas composition, which can be calculated as:

$$HV_{i,k} = \sum_{n \in \mathcal{N}} HV_n \phi_{i,k,n} \quad (5)$$

$$S_{i,k} = \sum_{n \in \mathcal{N}} M_n \phi_{i,k,n} / M^{air} \quad (6)$$

where $\mathcal{N}$ is the set of gas components; HV_n and M_n are the heat value and molecular weight of component n relative to air, respectively; $\phi_{i,k,n}$ is the concentration of component n.

3. MPOEF model

When the renewable generation fluctuates, the alternative gas injection will also fluctuate, which may cause the gas compositions to violate the secure range. The MPOEF model is then developed to accommodate the alternative gas injection securely. MPOEF aims to minimize the total cost C^T over the operational horizon, by changing the real-time operation status of gas sources, PTGs, GPPs, conventional fossil units, renewable generations, etc., as shown below:

$$C^T = \sum_{k \in \mathcal{K}} \left(\sum_{i \in \mathcal{I}} \sum_{l \in \mathcal{L}_i^{cpp}} cst_{i,l}(g_{i,l,k}^{cpp}) + \sum_{i \in \mathcal{I}} \sum_{l \in \mathcal{L}^s} \mu_{i,l}^s Q_{i,l,k}^s \right) \quad (7)$$

where $\mathcal{I}$ is the set of gas nodes; $\mathcal{L}_i^{cpp}$ and $\mathcal{L}_i^s$ are the sets of conventional fossil units and gas well at node i, respectively; $g_{i,l,k}^{cpp}$ is the electricity generation of conventional fossil unit l at node i in time k; $Q_{i,l,k}^s$ is the gas production of gas source l at node i at time k; $cst_{i,l}$ is the cost of conventional fossil unit l at node i; $\mu_{i,l}^s$ is the unit gas price.

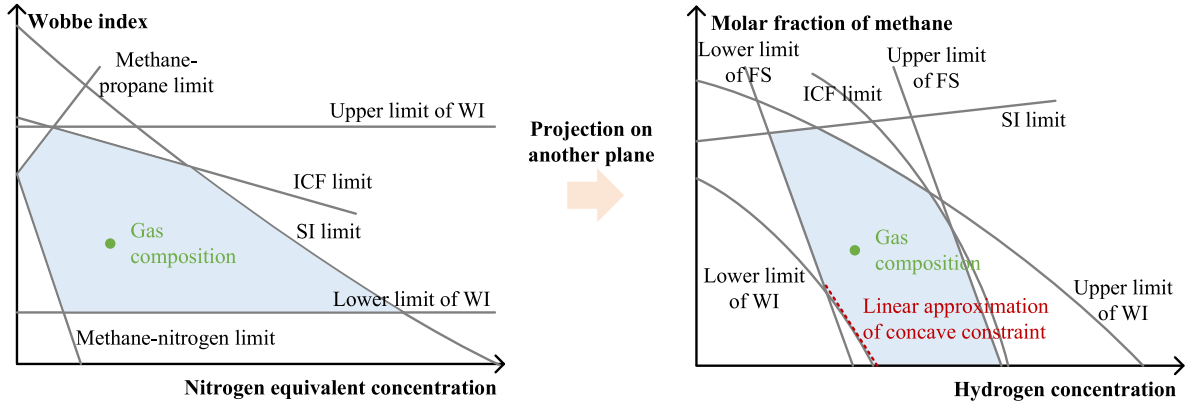In the following subsections, the constraints of the MPOEF problem will be modelled in detail.

Fig. 2. Security ranges for gas composition using Dutton diagram.

3.1. Model of gas system

3.1.1. Model of the gas system dynamics

In a horizontal and isothermal pipeline, the gas mixture flow is governed by the following three sets of PDEs, i.e., continuity, motion, and advective transport equation [41,42]. We use the finite difference scheme to discretize these PDEs. Specific derivations can be found in Appendix A.

$$\frac{A_{ij}}{\rho_0}\frac{\Delta\rho^t_{ij,s,k}}{\Delta t} + \frac{\Delta Q^x_{ij,s,k}}{\Delta x} = 0 \tag{8}$$

$$\frac{\Delta p^x_{ij,s,k}}{\Delta x} + \frac{\rho_0}{A_{ij}}\frac{\Delta Q^t_{ij,s,k}}{\Delta t} + \gamma_{ij}\Theta^2\frac{\overline{Q}^2_{ij,s,k}}{\overline{\rho}_{ij,s,k}} = 0 \tag{9}$$

$$\frac{\Delta\phi^t_{ij,s,k,n}}{\Delta t} + \frac{\rho_0}{A_{ij}}\frac{\overline{Q}_{ij,s,k}}{\overline{\rho}_{ij,s,k}}\frac{\Delta\phi^x_{ij,s,k,n}}{\Delta x} = 0,$$

$$ij \in \mathcal{GP}, s \in S, k \in \mathcal{K}, n \in \mathcal{N} \tag{10}$$

where $\Delta\rho^t_{ij,s,k}$, $\Delta Q^t_{ij,s,k}$, and $\Delta\phi^t_{ij,s,k,n}$ are the discretized terms of gas density, gas flow, and gas composition in the segment s of pipeline ij (the pipeline that connects gas bus i and j) at time k over the time dimension, respectively; $\Delta p^x_{ij,s,k}$, $\Delta Q^x_{ij,s,k}$, and $\Delta\phi^x_{ij,s,k,n}$ are the discretized terms of gas pressure, gas flow, and gas composition in the segment s of pipeline ij at time k over the space dimension; $\overline{Q}_{ij,s,k}$ and $\overline{\rho}_{ij,s,k}$ are the average value of gas flow and gas density in segment s in pipline ij at time k; A_{ij} is the cross-section area of the pipeline ij; ρ_0 is the gas density of the pure natural gas in the standard temperature and pressure condition; $\Theta^2_{ij} = \frac{8f_{ij}\rho^2_0}{\pi^2 D^5_{ij}}$, where f_{ij} and D_{ij} are the Fanning coefficient and diameter of pipeline ij, respectively [43]; $\mathcal{GP}$ is the set of gas pipelines; S is the set of pipeline segments; $\mathcal{K}$ and $\mathcal{N}$ are the sets of time steps during the operation and gas compositions, respectively; Δt and Δx are the temporal and spatial resolutions, respectively; $\gamma_{ij} = sgn(Q_{ij}|_{t=0})$ is the gas flow direction at $t = 0$; $sgn(\cdot)$ is the signum function.

When the gas composition changes, we assume the temperature remains stable. This is a reasonable assumption and widely used for hydrogen blending studies if we assume: (1) There is no phase transformation or chemical reaction between natural gas and hydrogen during the mixing process; (2) Gas pressures at the pipeline connection point (where the gas mixing happens) are the same; (3) No heat exchange between the gas in the pipelines and the environment outside the pipelines. With these assumptions, according to the ideal gas law, even if the gas composition changes dynamically, we can still assume the temperature does not change during the gas mixing. Then, according to the state equation of gas, the density and pressure of the gas should obey:

$$p_{ij,s,k} = z_{ij,s,k}r_{ij,s,k}T_0\rho_{ij,s,k} \tag{11}$$

where $z_{ij,s,k}$, $r_{ij,s,k}$, and $\rho_{ij,s,k}$ are the compressibility factor, gas constant, and gas density at segment s in pipeline ij in time k, respectively; T_0 is the temperature of the gas mixture.

Different from the traditional gas system model with uniform gas concentration, the gas constant here is a variable depending on the gas composition:

$$r_{ij,s,k} = \sum_{n\in\mathcal{N}}\phi_{ij,s,k,n}R_n \tag{12}$$

where $\phi_{ij,s,k,n}$ is the gas composition of gas component n; R_n is the gas constant of gas component n.

3.1.2. Initial, boundary, and terminal conditions

Firstly, initial and boundary conditions need to be specified. The initial condition is the state of gas system when $t = 0$ (i.e., $p_{ij,s,1} = \hat{p}_{ij,s}$, $Q_{ij,s,1} = \hat{q}_{ij,s}$, $\phi_{ij,s,1,n} = \hat{\phi}_{ij,s,n}$, where $\hat{p}_{ij,s}$, $\hat{q}_{ij,s}$, and $\hat{\phi}_{ij,s}$ can be calculated according to [16]).

The boundary conditions of the pipeline are determined by the pipelines and components that it connects with. Eq. (13) and (14) show the consistency of gas pressure at pipeline connecting points. Eq. (15) describes the nodal gas conservation for each gas component. Eqs. (16) and (17) describe that the gas compositions of pipelines at the connection point should be the same.

$$p_{ij,1,k} = p_{i,k} = p_{ij',1,k}, \forall j' \in \mathcal{J}_i \tag{13}$$

$$p_{ij,S,k} = p_{j,k} = p_{i'j,S,k}, \forall i' \in \mathcal{I}_j \tag{14}$$

$$\sum_{l\in\mathcal{L}^s_i}Q^s_{i,l,k,n} - Q^d_{i,k,n} + \sum_{l\in\mathcal{L}^{ptg}_i}Q^{ptg}_{i,l,k,n} - \sum_{l\in\mathcal{L}^{gpp}_i}Q^{gpp}_{i,l,k,n}$$

$$- \sum_{j\in\mathcal{J}_i}Q_{ij,1,k,n} = 0, \forall n \in \mathcal{N} \tag{15}$$

$$(\gamma_{ij}+1)\phi_{ij,1,k,n} = (\gamma_{ij}+1)\phi_{i,k,n}, \forall n \in \mathcal{N} \tag{16}$$

$$(\gamma_{ij}-1)\phi_{ij,S,k,n} = (\gamma_{ij}-1)\phi_{j,k,n}, \forall n \in \mathcal{N} \tag{17}$$

where $p_{ij,1,k}$ and $p_{ij,S,k}$ represents the gas pressure at the 1st and S_{th} segments in pipeline ij in time k, respectively; $p_{i,k}$ is the nodal pressure at node i in time k; $\mathcal{J}_i$ and $\mathcal{I}_j$ are the sets of nodes connect with node i and node j, respectively; $Q^d_{i,k,n}$ is the demand of gas component n at node i; $\mathcal{L}^{gpp}_i$ and $\mathcal{L}^{ptg}_i$ are the set of GPPs and PTGs at node i, respectively; $Q^{gpp}_{i,l,k,n}$ is the gas consumption from GPP l in node i in time k; $Q^{ptg}_{i,l,k,n}$ are the gas production of PTG l at node i in time k; $\phi_{ij,1,k,n}$ and $\phi_{ij,S,k,n}$ are the gas composition of gas component n at the 1st and S_{th} segments in pipeline ij, respectively; $\phi_{i,k,n}$ is the gas composition at node i in time k.

Since the gas system operates continuously, it is essential to guarantee the terminal state of the gas system should not deviate too much from the initial states. Otherwise, the gas system will be vulnerable and cannot maintain its flexibility to withstand future risks. In the

traditional gas system with constant gas composition, the volume of the linepack is usually used as the terminal condition of the gas system control problems [44]. However, when the gas composition is varying, the energy contained in the same volume of gas may be different. Therefore, there we extend the linepack volume into linepack energy, which should be maintained over a certain level at the end of the MPOEF:

$$\zeta_{ij,k} = A_{ij}/\rho_0 \sum_{s \in S} \sum_{n \in \mathcal{N}} HV_n \rho_{ij,s,k,n} \phi_{ij,s,k,n} \Delta x_{ij} \quad (18)$$

$$\zeta_{ij,K} \geq (1 - \beta^{lp})\zeta_{ij,0} \quad (19)$$

where $\zeta_{ij,k}$ is the linepack energy at time k; β^{lp} is the threshold coefficient, which is set to maintain the level of linepack energy; K is the total time steps.

3.1.3. Models of the gas demand and gas source

Considering that gas demand primarily entails combustion, the heat energy associated with the gas demand should remain consistent despite variations in gas compositions. Additionally, the gas composition at a specific node should match the gas composition of the gas demand at that node. Therefore, we have:

$$HV^{ng} q_{i,k}^{d,ng} = \sum_{n \in \mathcal{N}} Q_{i,k,n}^d HV_n, \quad q_{i,k,n}^d \geq 0 \quad (20)$$

$$Q_{i,k,n}^d = \phi_{i,k,n} \sum_{n \in \mathcal{N}} Q_{i,k,n}^d \quad (21)$$

where HV^{ng} is the heat value of natural gas; $Q_{i,k}^{d,ng}$ is the original gas demand in natural gas flow rate in time k.

Considering the different gas concentrations of gas sources, it can be modelled as:

$$Q_{i,l,k,n}^s = \phi_{i,l,n}^s Q_{i,l,k}^s, \quad \sum_{n \in \mathcal{N}} \phi_{i,l,k,n}^s = 1, \quad (22)$$

$$Q_{i,l}^{s,min} \leq Q_{i,l,k}^s \leq Q_{i,l}^{s,max} \quad (23)$$

where $\phi_{i,l,n}^s$ is the concentration of the component n of gas source l at node i; $q_{i,l}^{s,max}$ and $q_{i,l}^{s,min}$ are the maximum and minimum values of the gas supply, respectively.

3.1.4. Model of gas network

The gas at a node comes from the upper stream components (i.e., upstream pipelines, natural gas sources, PTGs). These gases may have different gas compositions. They will be mixed uniformly at this gas node, and flow to downstream components (i.e., downstream pipelines, gas loads, GPPs). To model this process, we calculate the total gas injection into gas node i of each/all component(s) $Q_{i,k,n}^{in}/Q_{i,k}^{in}$:

$$Q_{i,k,n}^{in} = \sum_{j \in \mathcal{J}_i} \frac{(1 - \gamma_{ij})}{2} Q_{ij,1,k,n} + \sum_{j \in \mathcal{J}_i} \frac{(1 + \gamma_{ji})}{2} Q_{ij,S,k,n} + \sum_{l \in \mathcal{L}_i^s} Q_{i,l,k,n}^s$$
$$+ \sum_{l \in \mathcal{L}_i^{ptg}} Q_{i,l,k,n}^{ptg} \quad (24)$$

$$Q_{i,k}^{in} = \sum_{n \in \mathcal{N}} Q_{i,k,n}^{in} \quad (25)$$

Then, we have:

$$\phi_{i,k,n} = Q_{i,k,n}^{in}/Q_{i,k}^{in}, \quad (26)$$

3.1.5. Other trivial constraints

Besides the above constraints, there are other trivial constraints required for the gas system to solve the MPOEF problem:

$$Q_{ij,s,k} = \sum_{n \in \mathcal{N}} Q_{ij,s,k,n} \quad (27)$$

$$|Q_{ij,s,k}| \leq Q_{ij}^{max} \quad (28)$$

$$p_{ij}^{min} \leq p_{ij,s,k} \leq p_{ij}^{max} \quad (29)$$

$$\phi_{ij,s,k} \sum_{n \in \mathcal{N}} Q_{ij,s,k,n} = Q_{ij,s,k,n} \quad (30)$$

where Q_{ij}^{max} is the transmission capacity of pipeline ij; p_{ij}^{max} and p_{ij}^{min} are boundaries for the gas pressure in pipeline ij, respectively.

3.2. Model of coupling components

3.2.1. Power-to-gas facility

PTG facilities play a pivotal role in IEGS by converting surplus renewable electricity into methane/hydrogen. It can be modelled as:

$$g_{i,l,k}^{ptg} \eta_{i,l}^e = Q_{i,l,k}^{me} HV^{me}/\eta_{i,l}^{me} + Q_{i,l,k}^{hy} HV^{hy} \quad (31)$$

$$Q_{i,l}^{hy} \geq 0, Q_{i,l}^{me} \geq 0 \quad (32)$$

$$0 \leq g_{i,l,k}^{ptg} \leq g_{i,l}^{ptg,max} \quad (33)$$

where $g_{i,l,k}^{ptg}$ is the electricity demand of PTG l; $\eta_{i,l}^e$ and $\eta_{i,l}^{me}$ are the efficiencies of electrolysis and mathenation processes, respectively; HV^{hy} and HV^{me} are the heat values of hydrogen and methane, respectively; $Q_{i,l,k}^{hy}$ and $Q_{i,l,k}^{me}$ are the hydrogen and methane productions of PTG l at node i in time k, respectively; $g_{i,l}^{ptg,max}$ is the PTG capacity.

3.2.2. Gas-fired power plants

The gas composition of the mixture consumed by GPP for electricity generation should align with the gas composition at the respective gas node. Thus, we have:

$$g_{i,l,k}^{gpp} = \eta_{i,l}^{gpp} \sum_{n \in \mathcal{N}} Q_{i,l,k,n}^{gpp} HV_n, \quad Q_{i,l,k,n}^{gpp} \geq 0 \quad (34)$$

$$Q_{i,l,k,n}^{gpp}/\sum_{n \in \mathcal{N}} Q_{i,l,k,n}^{gpp} = \phi_{i,k,n} \quad (35)$$

where $g_{i,l,k}^{gpp}$ and $\eta_{i,l}^{gpp}$ are the power output and efficiency of the GPP l, respectively; $Q_{i,l,k,n}^{gpp}$ is the consumption of gas component n by the GPP.

3.3. Model of the power system

In the transmission level energy system, the resistance of the power line is much smaller than the reactance and can be neglected. Without sacrificing accuracy, the DC model has higher computation efficiency and robustness, which has been widely used by the power system operator for optimal dispatch, market clearing and unit commitment [45,46]. Therefore, here we use the DC optimal power flow model [47]:

$$\sum_{l \in \mathcal{L}_i^{cpp}} g_{i,l,k}^{cpp} + \sum_{l \in \mathcal{L}_i^{gpp}} g_{i,l,k}^{gpp} + \sum_{l \in \mathcal{L}_i^{rng}} g_{i,l,k}^{rng} - \sum_{l \in \mathcal{L}_i^{ptg}} g_{i,l,k}^{ptg}$$
$$-g_{i,k}^d - \sum_{j \in \mathcal{J}_i} g_{ij,k} = 0 \quad (36)$$

$$g_{ij,k} = (\theta_{i,k} - \theta_{j,k})/X_{ij} \quad (37)$$

$$|g_{ij,k}| \leq g_{ij}^{max} \quad (38)$$

$$g_{i,l}^{cpp,min} \leq g_{i,l,k}^{cpp} \leq g_{i,l}^{cpp,max} \quad (39)$$

$$g_{i,l}^{gpp,min} \leq g_{i,l,k}^{gpp} \leq g_{i,l}^{gpp,max} \quad (40)$$

$$g_{i,l,k}^{rng,min} \leq g_{i,l,k}^{rng} \leq g_{i,l,k}^{rng,max} \quad (41)$$

where $\mathcal{L}_i^{rng}$ represents renewable generators at node i, and $g_{i,l,k}^{rng}$ is its power output; $g_{i,k}^d$ is the power demand at node i in time k; $g_{ij,k}$ is the electric power flow on branch ij in time k; $\theta_{i,k}$ is the phase angle of the voltage; X_{ij} is the reactance; g_{ij}^{max} is the transmission capacity; $g_{i,l}^{cpp,max}$, $g_{i,l}^{cpp,min}$, $g_{i,l}^{gpp,max}$, $g_{i,l}^{gpp,min}$, $g_{i,l}^{rng,max}$, and $g_{i,l}^{rng,min}$ are the boundaries of conventional fossil units, GPPs, and wind generations, respectively.

4. Solution method

4.1. SOC reformulation of MPOEF problem

The nonconvexity of the above MPOEF lies in these three sets of constraints: (1) the discretized form of the PDEs, such as the quadratic-over-linear terms in (9) and (10). (2) the bilinear terms in the gas state Eq. (11), gas composition limits for gas demands (21) and GPPs (35), linepack terminal conditions (18), as well as the gas mixing Eqs. (26).

For the first nonconvexity regarding the gas flow dynamics, although the SOC relaxation technique has been introduced to convexify the gas flow equations with constant compositions [48], this technique cannot be applied to our models with variant gas compositions. This is because the gas constant $r_{ij,s,k}$ can no longer be considered as a constant, and thus the gas pressure and gas density do not hold a simple linear relationship according to (11). To tackle this problem, we develop the new SOC relaxation technique to convexify the gas flow dynamics model. For conciseness, here we rewrite m_{th} discretized motion Eqs. (9) or advective transport Eqs. (10) in a general form:

$$c_{m,h} \sum_{h \in \mathcal{H}} x_{m,h} y_{m,h} = 0 \tag{42}$$

where h and $\mathcal{H}$ are the index and set of all bilinear terms in the equation. For instance, in discretized motion equations, $\mathcal{H} = \{1, 2, 3\}$, and in discretized advective transport equation, $\mathcal{H} = \{1, 2\}$; $c_{m,h}$ is the coefficient of each bilinear term; $x_{m,h}$ and $y_{m,h}$ are the variables (such as $\bar{\rho}_{ij,s,k}$, $\Delta p^x_{ij,s,k}$, etc.).

Then, by introducing an auxiliary variable $\psi_{m,h}$, it can be reformulated and replaced by four constraints, including two SOC constraints and two linear constraints based on Taylor expansion, and the derivation process is introduced in Appendix B:

$$c_{m,h} \sum_{h \in \mathcal{H}} (x_{m,h} + y_{m,h})^2 \leq \psi^2_{m,h} \tag{43}$$

$$c_{m,h} \sum_{h \in \mathcal{H}} (x_{m,h} - y_{m,h})^2 \leq \psi^2_{m,h} \tag{44}$$

$$c_{m,h} \sum_{h \in \mathcal{H}} (x^*_{m,h} + y^*_{m,h})^2 + 2(x^*_{m,h} + y^*_{m,h})$$
$$((x_{m,h} + y_{m,h}) - (x^*_{m,h} + y^*_{m,h})) + \delta_{m,h} \geq \psi^2_{m,h} \tag{45}$$

$$c_{m,h} \sum_{h \in \mathcal{H}} (x^*_{m,h} - y^*_{m,h})^2 + 2(x^*_{m,h} - y^*_{m,h})$$
$$((x_{m,h} - y_{m,h}) - (x^*_{m,h} - y^*_{m,h})) + \delta_{m,h} \geq \psi^2_{m,h} \tag{46}$$

where $x^*_{m,h}$ and $y^*_{m,h}$ are the reference values of $x_{m,h}$ and $y_{m,h}$, respectively; $\psi_{m,h}$ is the slack variable for the Taylor remainder. The selection of reference values will be introduced in the next subsection in the solution procedures. The specific reformulations of motion and advective transport equations can be found in the Appendix C.

The bilinear term in (11) is now approximated as:

$$p_{ij,s,k} = z_{ij,s,k} T_0 \left(r^*_{ij,s,k} \rho^*_{ij,s,k} + r^*_{ij,s,k}(\rho_{ij,s,k} - \rho^*_{ij,s,k}) + (r_{ij,s,k} - r^*_{ij,s,k})\rho^*_{ij,s,k} \right) + \delta^{es}_{ij,s,k} \tag{47}$$

where $\delta^{es}_{ij,s,k}$ is the Taylor remainder of (47). It can also be incorporated into the framework of sequential programming. Other bilinear constraints can be handled similarly.

4.2. Sequential SOC programming procedures

The basic idea of sequential programming is that, by controlling the slack variables, the optimization problem can be convexified and solved with some constraints violations initially, and then converged to the optimum as iteration proceeds. The specific procedures are as follows:

Step 1: Set IEGS parameters and collect wind speed data. Initialize the length and time resolutions for PDEs. Initialize the penalty $\beta^{mo,(0)}$,
$\beta^{at,(0)}$, $\beta^{at,(0)}$, $\beta^{es,(0)}$, and $\beta^{re,(0)}$, as well as their upper bounds $\beta^{mo,max}$, $\beta^{at,max}$, $\beta^{es,max}$, $\beta^{re,max}$. Set the residual tolerance for the sequential programming ϵ.

Step 2: For each time k, given the wind speed, solve the steady-state-based optimal energy flow problem with alternative gas injections according to [16]. Set the solutions at $k = 1$ as the initial condition for PDEs. Set the solutions at each time k as the initial reference values for the sequential programming. Set the iteration index for sequential programming $v = 1$.

Step 3: In the v_{th} iteration, solve the following SOC programming problem by the given reference points:

$$\begin{aligned}
\min \quad y^{(v)} = C^T &+ \sum_{k \in \mathcal{K}} \Bigg(\sum_{(ij) \in \mathcal{GP}} \sum_{s \in S} \bigg(\lambda^{mo}(\psi^{mo}_{ij,s,k})^2 + \beta^{mo,(v)} \delta^{mo,(v)}_{ij,s,k} \\
&+ \beta^{se,(v)} \delta^{se,(v)}_{ij,s,k} \\
&+ \sum_{n \in \mathcal{N}} (\lambda^{at}(\psi^{at}_{ij,s,k,n})^2 + \beta^{at,(v)} \delta^{at,(v)}_{ij,s,k,n}) \bigg) + \sum_{i \in \mathcal{I}} \sum_{n \in \mathcal{N}} \beta^{re,(v)} \delta^{re,(v)}_{i,s,n,k} \Bigg)
\end{aligned} \tag{48}$$

where λ^{mo} and λ^{at} are the penalty coefficients for motion and advective transport equations, respectively. It subjects to: (11)–(47) and $\phi_{i,k} \in \mathbb{H}$ (as defined in Section 2). By solving the problem above, the solution in v_{th} iteration can be obtained.

Step 4: Check if all the state variables of the IEGS do not change compared with the last iteration, and if all the Taylor remainders converge to zero. For example:

$$|y^{(v)} - y^{(v-1)}|/(y^{(v)} + y^{(v-1)}) \leq \epsilon \tag{49}$$

$$\sum_{k \in \mathcal{K}} \Bigg(\sum_{(ij) \in \mathcal{GP}} \sum_{s \in S} \bigg(\delta^{mo,(v)}_{ij,s,k} + \sum_{n \in \mathcal{N}} \delta^{at,(v)}_{ij,s,k,n} + \beta^{se,(v)} \delta^{se,(v)}_{ij,s,k} \bigg) + \sum_{i \in \mathcal{I}} \sum_{n \in \mathcal{N}} \delta^{re,(v)}_{i,s,n,k} \Bigg) \leq \epsilon \tag{50}$$

If yes, end the sequential programming and output the solution as the final result. If no, set the solution in v_{th} iteration as the reference value. Update the penalty coefficients as follows (other penalty coefficients can be updated similarly), and return to **Step 3**.

$$\beta^{mo,(v+1)} = \min \left\{ \vartheta \beta^{mo,(v)}, \beta^{mo,max} \right\} \tag{51}$$

where ϑ is the multiplier for the penalty coefficients.

5. Case studies

In the case study, we validate our MPOEF scheme and the corresponding solution method by using IEEE 24 RTS [49] and the Belgium gas transmission system [50]. The Belgium gas system is selected for validation because it has similar annual gas demand, gas consumption structures, and gas network structures with other European countries. Therefore, the results and findings can be representative. Several modifications are introduced, enhancing the representations of real-world scenarios: (1) The two energy systems are interconnected based on the topology illustrated in Fig. 3; (2) To align with the integrated nature of the system, traditional generators (#1, 2, 5, 6, 9–11, and 16–20) are replaced with GPPs. Refer to [49] for the original indices of these generators. (3) the generator #23 is replaced by an 800 MW wind farm; (4) PTG facilities have hydrogen production capacities of 2 Mm^3/day. The detailed system data used in this paper can be found in [51] Penalty factors of motion equation and active transport equation are set as 10, i.e., $\lambda^{mo} = \lambda^{at} = 10$; The initial values of penalty coefficients for Taylor remainders are set as 1, i.e., $\beta^{mo,(0)} = \beta^{se,(0)} = \beta^{at,(0)} = \beta^{re,(0)} = 1$; The multiplier for penalty coefficient during each iteration $\vartheta = 2$; Upper bounds for penalty coefficients are set as 10^4; criterion for convergence $\epsilon = 10^{-3}$. The simulation period is 24 h. The optimization is performed on a Lenovo laptop.
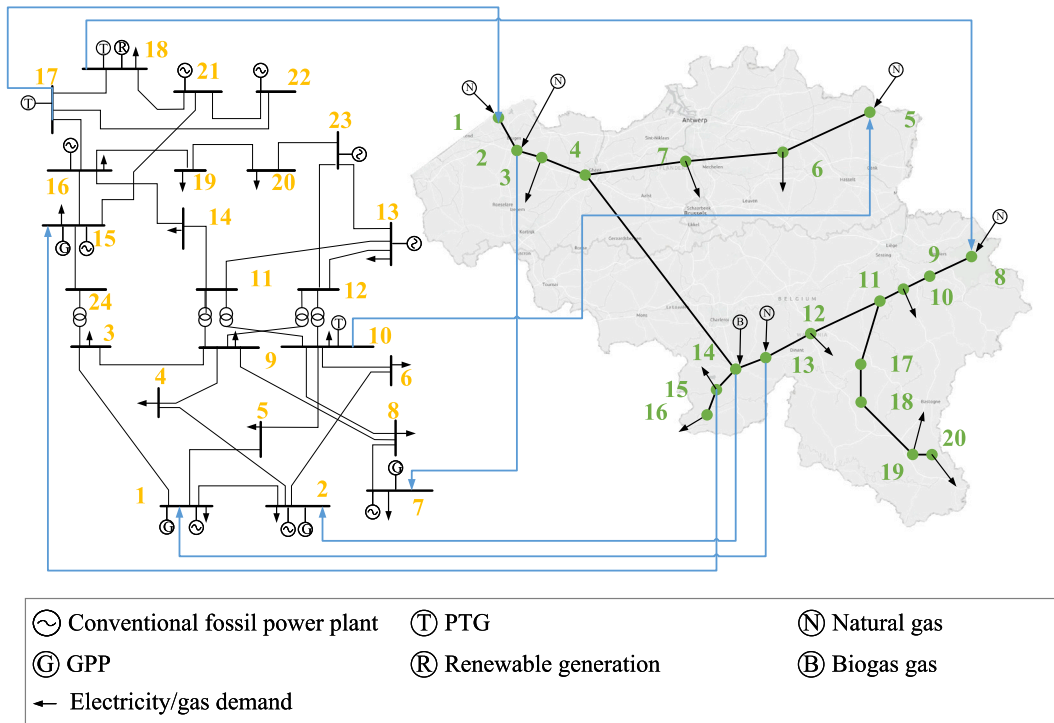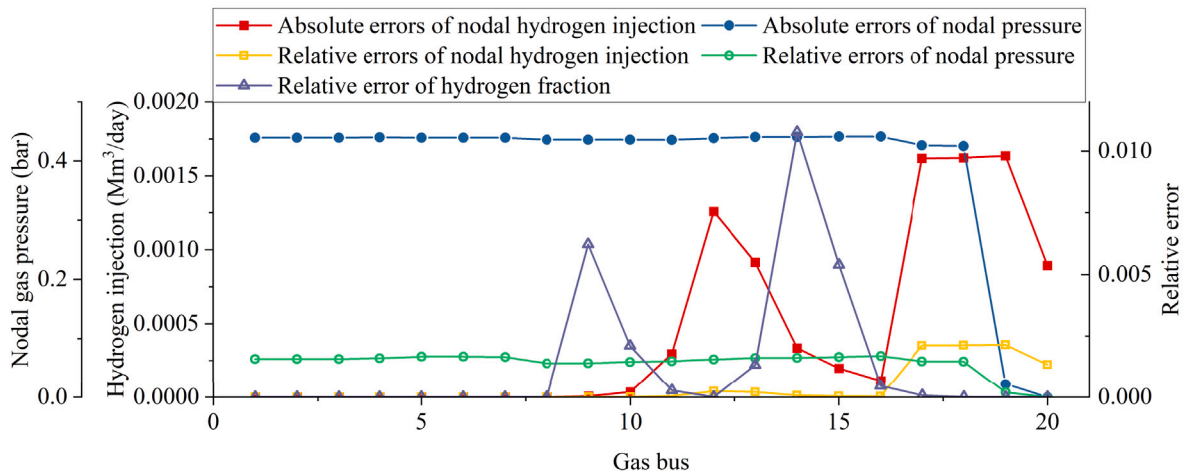
Fig. 3. IEGS test system.

Fig. 4. Accuracy of the solution method.

5.1. Validation of proposed solution method

5.1.1. Selections of time and length steps

Four scenarios S1-S4 are compared to determine the appropriate time and length of steps for discretizing PDEs. In this case, the PTG at gas node #8 is committed. we set the dispatchable capacity of the renewable generators equals zero at $t = 0$, i.e., $g_{i,l,k}^{rng,max} = 0, k = 1$, and equals 800 MW after one hour, i.e., $g_{i,l,k}^{rng,max} = 800, k = 3$ (time step is 1800 s). Then, the initial condition of the gas system variables (including gas pressure, gas flow, etc.) at $t = 0$ is determined by implementing steady-state optimal energy flow of IEGS with hydrogen injection using the method described in [16]. The boundary conditions are set according to Section 3.1.2. The settings of the four scenarios are marked in Fig. 5. The computation times for these four scenarios are 35.88, 29.82, 22.13, and 12.32 s, respectively.

We take S1 as the baseline. As we can see, with the increase in the length step, the relative error increases. The error in S2 is relatively small, and the average value is 5.30×10^{-4} during the whole transient process. However, as the length step increases to 50000 m, the mean relative error increases to 0.18%, and conviction oscillations occur. We also observed that the maximum error occurs at the beginning, as shown by the purple dash line in S3. The maximum error could be up to 2.58%. In contrast, the dotted line in S2 is always very close to the baseline throughout the transient process. The computation times of these three scenarios are relatively close. Therefore, judging by the accuracy, here we select the size of the length step as 10000 m.
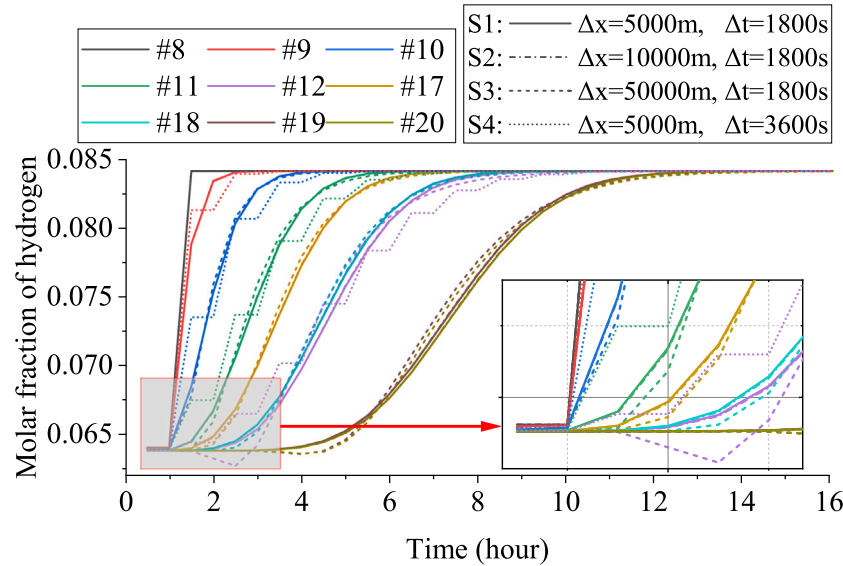
Fig. 5. Comparison of different time and length steps.

Table 1
Comparison of computation performance.

Method	Method A	Method B	Method C
Computation time (s)	1264	221.9	29.82
Average relative error	/	0.00095	0.0013

The selection of the time mainly depends on the required time resolution. We also notice an unneglectable error between S1 and S4, especially just before the concentration of hydrogen approaches the steady-state value. Thus, in the following case studies, the time step Δt is selected as 1800 s.

5.1.2. Computation performance

To demonstrate the superiority of our proposed method, we compare it with other methods in this section. Our method (Method C) is to reformulate the original problem into SOC optimization problems and is solved with the MOSEK solver. In Method A, the optimization problem remains in its original form, and is solved by a general nonlinear solver IPOPT. In Method B, the nonlinearities other than bilinearities are reformulated, and the resulting bilinear optimization problem is solved by the latest version of Gurobi using the dynamic outer approximation technique [52]. The relative error and computation time are shown in Table 1.

By averaging the results in 100 stochastic scenarios, we can find our method takes 29.82 s to obtain the results, 42 times faster than the IPOPT. Moreover, regarding the solutions of the nonlinear solver as the baseline, the absolute and relative errors at different gas nodes, in terms of nodal hydrogen injection, gas pressure, and hydrogen fraction, with our method are shown in Fig. 4. As we can see, the mean error is only around 0.13%. The absolute errors of nodal hydrogen injections and gas pressures can be controlled within 0.0018 Mm^3/day and 0.45 bar, respectively, and the relative errors can be controlled within 1.1%. The maximum relative error appears at gas node #14 where the gases are mixed. Compared with Method B, though the error of our method is a little higher (both methods are accurate enough within the converging tolerance), our computation efficiency is 7.44 times higher.

5.2. Travelling of alternative gas

Secondly, our MPOEF scheme in tracking the travelling of alternative gas concentrations is investigated. It is similar to the last case, except that the wind generating capacity recovers to 0 MW at $t = 12$ h.

The propagation of the hydrogen content along the critical branch, i.e., from gas nodes #8–12 and #17–20, is presented in Fig. 6. As we can see, the hydrogen content that is injected into gas node #8 gradually travels to distant locations along the pipeline route. The concentration of hydrogen increases immediately to 8.43% after the injection at $t = 1$ h at gas node #8. In contrast, the concentration of hydrogen at gas node #20 reaches its maximum value at t = 13.5 h. The total settling time is 9 h. This indicates that considering the propagation time of hydrogen concentration in the MPOEF is very necessary. Otherwise, it will lead to miscalculations in the gas composition distribution in the gas system.

Several security indices, i.e., WI and FS, at the representative gas nodes, are further presented in Fig. 7. As we can see, these security indices are tightly dependent on the concentration of hydrogen. For instance, for gas nodes #8–12 and 17–20, when they reach the peak value of hydrogen concentration, the Wobbe indices become lowest (52.00 MJ/m^3). Although it is lower than the WI of original natural gas, it does not violate the lower limit (50.22 MJ/m^3). In contrast, the propagation of hydrogen content significantly impacts the FS. Many nodes, including #8–12 and 17–20, violate the upper bound temporarily after the hydrogen travels to their locations. This indicates that during operation, it is essential to track the real-time propagation of hydrogen concentrations to ensure gas security at the nodal level.

5.3. Demonstration of multi-period operation results

After validating our MPOEF method, it is employed for the multi-period operation in this section. All the PTGs are available in this section. The wind generation dispatchable capacities are set according to the wind data from [53]. The initial and boundary conditions are set according to the same principle in previous case studies. Three scenarios S1-S3 are compared. In S1, the security constraints are not considered. In S2 and S3, the security indices are limited to ±10% and ±5% of their values of original natural gas, respectively [54–56].

Observed from Fig. 8, generally in all the scenarios, the value of gas production of PTGs coincides with the trend of wind speed. For example, from 10:30–17:30, PTG #3 is operating at the maximum capacity because of the higher wind speed. Comparing different scenarios, we find that as the security limits become tighter, the hydrogen production of PTGs decreases. Instead, they choose to convert more hydrogen into methane, because methane has closer interchangeability compared to natural gas. For example, the total methane production in S1 is zero,
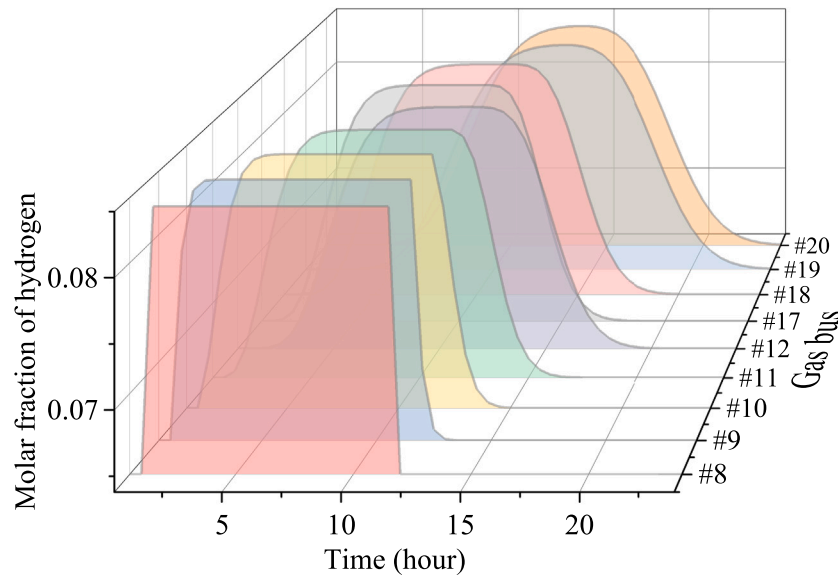
Fig. 6. Operating condition of IEGS: (a) PTG production; (b) travelling of the concentration of hydrogen.
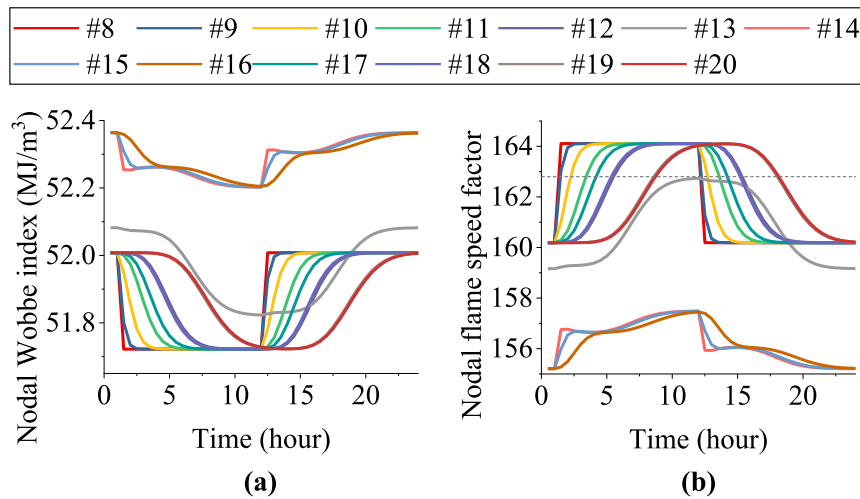

Fig. 7. Security indices: (a) WI; (b) FS.

while it increases to 9.85% in S2. This number further increases to 27.72% in S3.

The travelling of hydrogen in different critical pipeline routes, as well as the mixing process in S1, are demonstrated in Fig. 9(a)–(b). We find that the concentrations of hydrogen at injection points are in line with the hydrogen production of PTGs. For example, the concentration of hydrogen at gas node #1 increases from zero to around 20% immediately at 8:30, just when the hydrogen production of PTG #3 begins to increase. Then, as the hydrogen travels in the gas network, its concentration will be diluted both by mixing with pure natural gas (e.g., the gas source at gas node #2), or by the advection in the pipeline (e.g. gas node #3–4). It can also be diluted by gas mixing processes. For instance, the peak number of hydrogen concentration at gas node #4 is 10.98% at 17:30, which takes approximately 4.5 h to travel to gas node #14. At 22:00, it is diluted by the gas mixture from #13 (with 6.74% hydrogen). Then, the hydrogen concentration of the mixture at gas node #14 is reduced to 7.82%.

The security indices in three scenarios are compared in Fig. 9(c)–(d). We find that with more blended hydrogen, the WI will decrease, while the FS tends to increase. For instance, the WI at gas node #4 in S1 is 2.25% lower than that in S3. We also find that the FS is more

critical than the WI for the regulation of hydrogen injection. Even in S1, the WI does not violate the lower limit. On the contrary, in S2 and S3, the FS at gas node #11 reaches their upper bounds, respectively. It validates that our MPOEF successfully keeps these indices within the secured range, while the accommodation of green hydrogen can also be maximized. It also validates the necessity of adding the FS as an additional index to the traditional Dutton method, which can keep the security of a hydrogen-blended gas system.

The variations of linepack energies in these scenarios are demonstrated in Fig. 10. We can see that although the linepack energy varies with the wind power and hydrogen injection, they are still maintained within the acceptable range. For instance, in the pipeline that connects gas nodes #4–14, as shown in Fig. 10(a), the linepack energy decreases dramatically at 20:00 with the large volume of hydrogen injection. However, it recovers to the normal level at the end of the operation. We also find that with tighter security limits, the variation in the linepack is also minor. For instance, as illustrated in Fig. 10(b), the total linepack energy in the gas system at 24:00 in S3 is 4.07% higher than that in S1. Since the linepack energy is critical in maintaining the robustness of the gas network, the hydrogen injection can jeopardize that flexibility in some sense. Therefore, apart from the security indices, we should
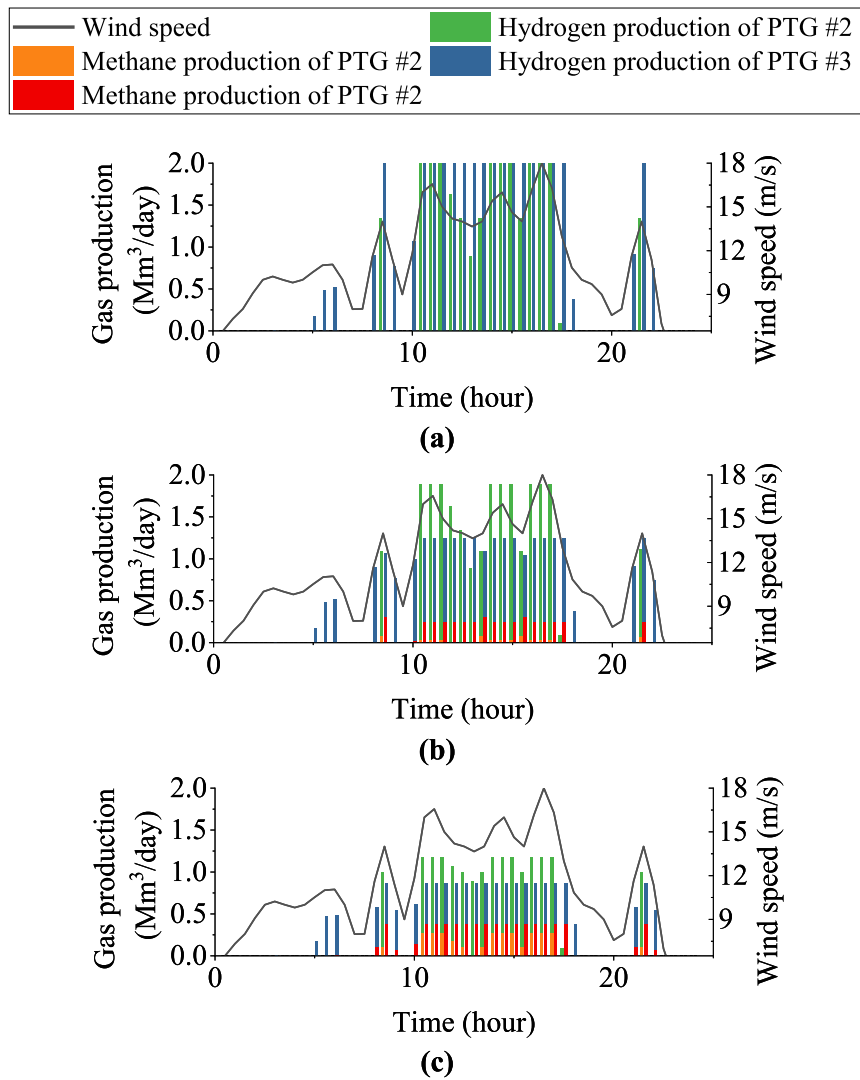
Fig. 8. Gas productions of PTGs: (a) S1; (b) S2; (c) S3.

also pay close attention to linepack energies when injecting hydrogen into the gas system.

5.4. Scalability of proposed solution method

To further demonstrate the effectiveness and scalability of our method, we compare the computation performance and demonstrate the results with a larger-scale China Northwest energy system.

The Northwestern China IEGS covers supplies the power and gas demand in Xinjiang, Qinghai, Gansu, Ningxia, and Shaanxi provinces, which is about 32.31% of the entire China's land area. Compared with Belgium IEGS, the Northwestern China IEGS is a typical inland and large-scale energy system. The Northwest China area is the most important natural gas production base, while also having rich endowments for solar and wind resources. Therefore, it would be an ideal test bed for hydrogen blending. The Northwestern China IEGS have 197 and 171 electricity and gas buses, respectively. The electricity and gas peak demands are 109.4 MW and 65.55 Mm³/day respectively. The detailed data of the energy system can be found in [51].

Our original 24-bus IEEE RTS power system and 20-bus Belgium gas system are considered as middle scale, denoted as E2 and G2, respectively. The original electricity and gas systems are abstracted into one node, and set as small-scale electricity system (E1) and gas system (G1), respectively. The Northwestern China electricity and gas systems

are denoted as E3 and G3, respectively. Three test scenarios are set to show the relationship between the scalability and system size, as shown in Table 2. S1 uses original combinations, i.e., E2-G2; S2 and S3 uses E1-G2 and E2-G1, respectively; S4 uses E3-G3. For illustration purposes, in all scenarios, we use the similar assumption as in Section 5.1 that the wind generation dispatchable capacities are zero at the beginning, and all reach their maximum capacity after one hour.

The computation times in four scenarios are presented in Table 2. We can find that the scale of the gas system is the main influencing factor of computation time. As we reduce the size of the gas system, the computation time reduces by 95.67%. Reducing the size of the electricity system can also save the computation time. When the scale of the energy system increases dramatically, the computation time also increases by around 21 times. Though this increase is ineglectable, our method still demonstrates its feasibility in large-scale systems, and the solution time frame is acceptable during operation or policy making, considering the complex nature of the optimization problem.

The evolution of hydrogen composition in China's Northwest IEGS during the operation is shown in Fig. 11. Natural gas and hydrogen generally flow from west to east. As we can see, due to the concentration of hydrogen injection by PTGs, the east areas have higher hydrogen fractions than the west. From $t = 0$ to $t = 120$ h, the hydrogen fraction in the east increases gradually. For example, at the border of Ganxu and Ningxia provinces, the hydrogen fraction is 10% at t = 30, but
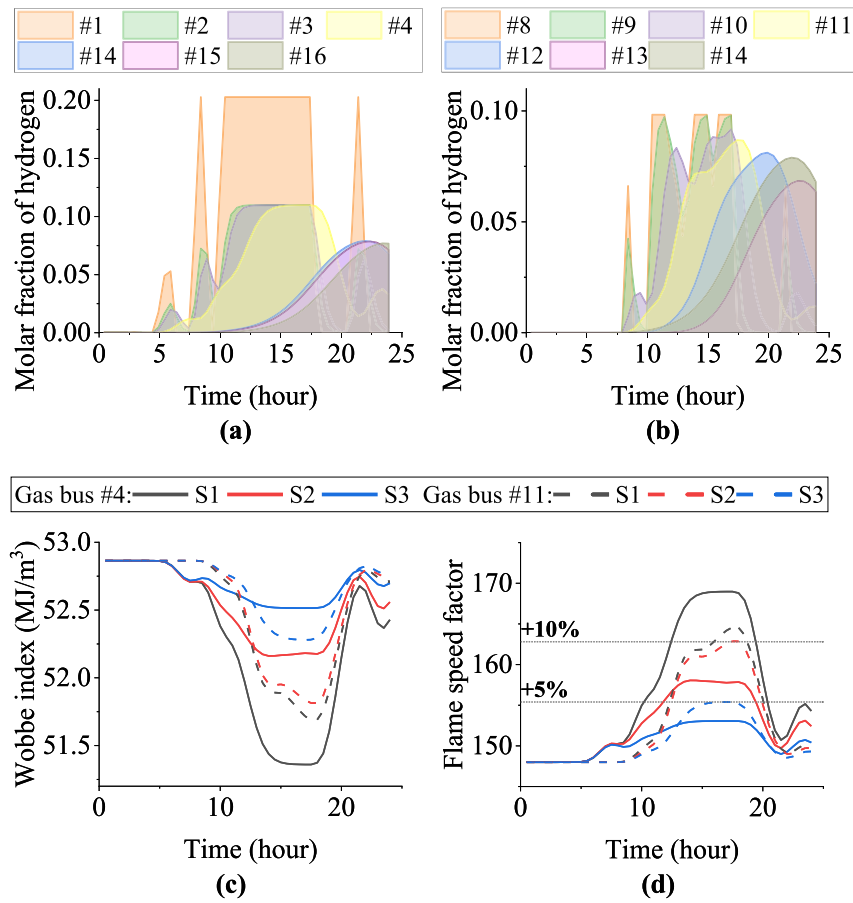
Fig. 9. Gas composition and security indices: (a) hydrogen concentrations at gas nodes#1-4-16; (b) hydrogen concentrations at gas nodes #8–14; (c) WI at gas nodes #4 and 11; (d) FS at gas nodes #4 and 11.
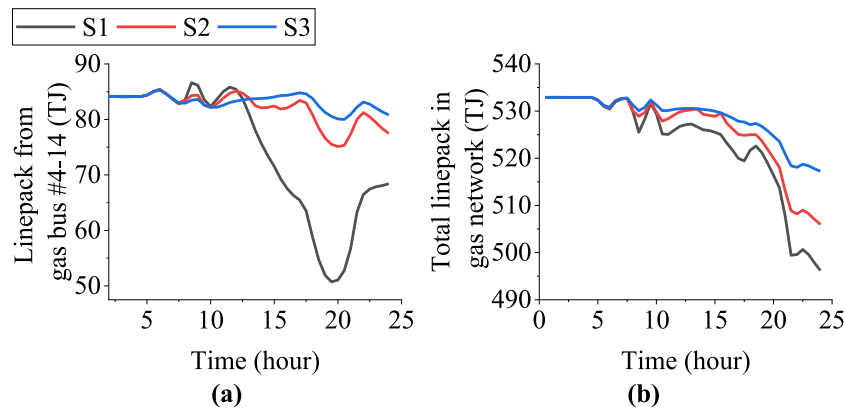

Fig. 10. (a) Linepack energies in the pipeline connecting gas nodes #4 and 14; (b) total linepack energies.

it increases to around 16% at t = 120. We can also observe that the high hydrogen areas only exist in Ningxia province at the beginning, but are expanded gradually to Ganxu and Shannxi. Nonetheless, this process takes 120 h to stabilize in large-scale China's energy systems, which further highlights the necessity of considering gas composition dynamics in hydrogen-blended energy systems.

6. Conclusions

This paper proposes an MPOEF model and a tractable solution method for IEGS with alternative gas. The dynamics of gas composition are characterized to reveal the travelling of hydrogen concentrations,

Table 2
Computation times of different scales of energy systems.

Scenario	E2-G2	E2-G1	E1-G2	E3-G3
Computation time (s)	29.82	1.29	16.11	622.1

as well as its influence on gas physical properties in real-time. Case studies demonstrate that our solution algorithm is 97.64% faster than general nonlinear solvers, while the deviation of accuracy is controlled within 1.1%. The MPOEF results show the necessity of considering the gas composition dynamics. The hydrogen content takes about 12.5 h to travel from the injection point to the end of the pipeline route.
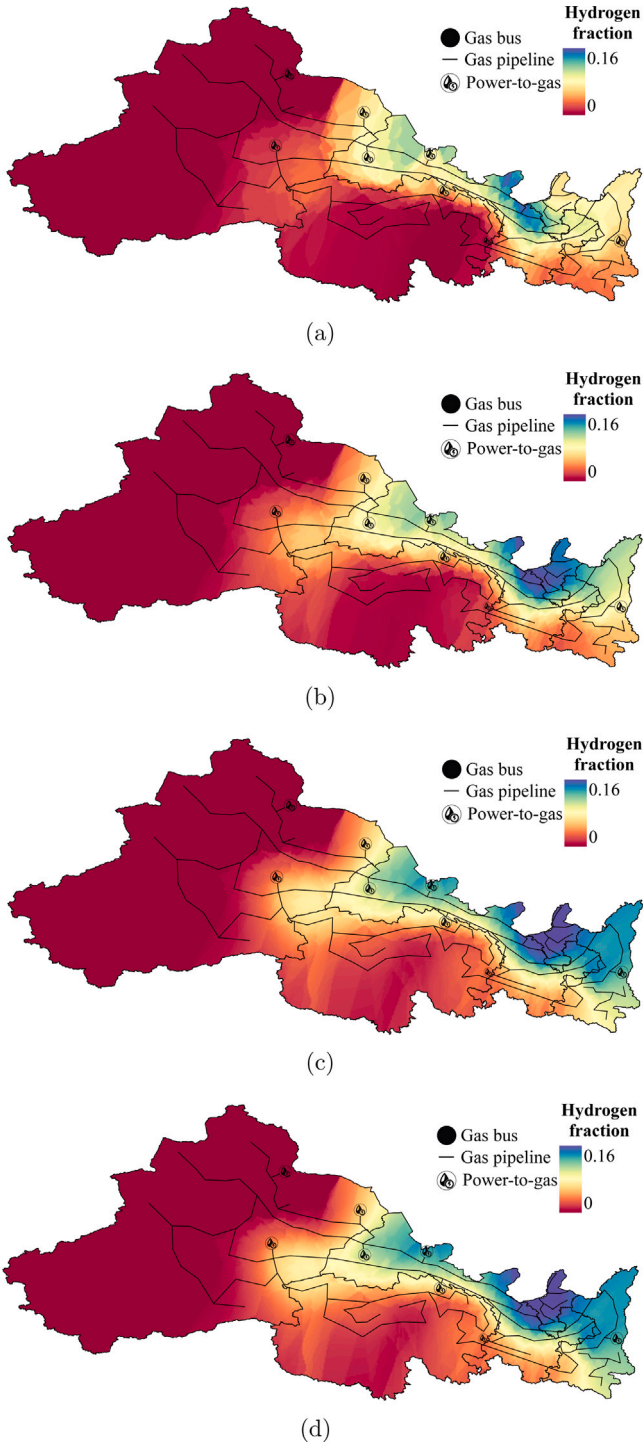
Fig. 11. Evolution of hydrogen compositions in China's Northwest IEGS: (a) t = 30 h; (b) t = 60 h; (c) t = 90 h; (d) t = 120 h.

Inaccuracies will be caused if we neglect this considerable travelling time. Moreover, we find that the FS is a more critical factor than other security indices. With different security limits, the accommodation of renewable energies, the gas production mode of PTGs, and the linepack energies will be different. A looser security limit will lead to a lower linepack energy, which may affect the flexibility of the gas system.

With the emerging policies and demonstration projects on hydrogen blending for decarbonization, the current energy systems are under pivotal changes. Our method can potentially be developed and used in practical energy systems for joint optimal dispatch and unit commitment, hydrogen pipeline expansion planning, and optimal sizing and allocation of PTGs in the hydrogen industry. We can further extend this fundamental model to incorporate the uncertainty of renewable energies using risk-hedging optimization frameworks such as distributionally robust optimization, and help the network operator to regulate the energy system safety during continuous operation. Our method also offers a powerful toolbox for policymakers to accurately and quantitatively assess the impact of hydrogen blending on energy systems, while optimizing their pathway to net zero.

CRediT authorship contribution statement

Sheng Wang: Writing – review & editing, Writing – original draft, Validation, Software, Methodology, Investigation, Formal analysis, Data curation, Conceptualization. **Hongxun Hui:** Writing – review & editing, Supervision, Resources, Project administration, Investigation, Funding acquisition, Data curation. **Tao Chen:** Writing – review & editing, Supervision, Resources, Investigation, Funding acquisition. **Junyi Zhai:** Writing – review & editing, Supervision, Resources.

Declaration of competing interest

The authors declare the following financial interests/personal relationships which may be considered as potential competing interests: Hongxun Hui reports financial support was provided by Science and Technology Development Fund, Macau SAR. If there are other authors, they declare that they have no known competing financial interests or personal relationships that could have appeared to influence the work reported in this paper.

Data availability

Data will be made available on request.

Acknowledgements

Appendix A. Discretization of PDEs of gas system dynamics

The original forms of the PDEs in (8)–(10) are:

$$\frac{A_{ij}}{\rho_0}\frac{\partial \rho_{ij}}{\partial t} + \frac{\partial Q_{ij}}{\partial x} = 0 \tag{A.1}$$

$$\frac{\partial p_{ij}}{\partial x} + \frac{\rho_0}{A_{ij}}\frac{\partial Q_{ij}}{\partial t} + \Theta_{ij}^2\frac{1}{\rho_{ij}}Q_{ij}|Q_{ij}| = 0 \tag{A.2}$$

$$\frac{\partial \phi_{ij,n}}{\partial t} + \frac{\rho_0}{A_{ij}}\frac{Q_{ij}}{\rho_{ij}}\frac{\partial \phi_{ij,n}}{\partial x} = 0, \ n \in \mathcal{N} \tag{A.3}$$

where p_{ij}, Q_{ij}, and ρ_{ij} are the pressure, flow rate, and density of the gas in pipeline ij, respectively; $\phi_{ij,n}$ is the gas composition of component n. These four variables are all functions of time t and location x.

The discretized and averaged terms in (8)–(10) are calculated by:

$$\bar{\rho}_{ij,s,k} = (\rho_{ij,s,k+1} + \rho_{ij,s+1,k+1})/2 \tag{A.4}$$

$$\Delta\rho_{ij,s,k}^t = (\rho_{ij,s,k+1} - \rho_{ij,s,k} + \rho_{ij,s+1,k+1} - \rho_{ij,s+1,k})/2 \tag{A.5}$$

$$\Delta Q_{ij,s,k}^x = Q_{ij,s+1,k+1} - Q_{ij,s,k+1} \tag{A.6}$$

$$\Delta Q_{ij,s,k}^t = (Q_{ij,s+1,k+1} - Q_{ij,s+1,k} + Q_{ij,s,k+1} - Q_{ij,s,k})/2 \tag{A.7}$$

$$\overline{Q}_{ij,s,k} = (Q_{ij,s,k} + Q_{ij,s+1,k} + Q_{ij,s,k+1} + Q_{ij,s+1,k+1})/4 \tag{A.8}$$

$$\Delta p^x_{ij,s,k} = p_{ij,s+1,k+1} - p_{ij,s,k+1} \tag{A.9}$$

$$\Delta \phi^t_{ij,s,k,n} = (\phi_{ij,s,k+1,n} - \phi_{ij,s,k,n} + \phi_{ij,s+1,k+1,n} - \phi_{ij,s+1,k,n})/2 \tag{A.10}$$

$$\Delta \phi^x_{ij,s,k,n} = \phi_{ij,s+1,k+1,n} - \phi_{ij,s,k+1,n} \tag{A.11}$$

where $Q_{ij,s,k}$ is the gas flow of segment s at time k.

Appendix B. Derivation of SOC constraints in general form

(42) can be split into two sides as follows. Then, let them both equal to the square of an auxiliary variable ($c_{m,h} \geq 0$):

$$c_{m,h} \sum_{h \in \mathcal{H}} (x_{m,h} + y_{m,h})^2 = c_{m,h} \sum_{h \in \mathcal{H}} (x_{m,h} - y_{m,h})^2 = \psi^2_{m,h} \tag{B.1}$$

Then, we can split each equation into one pair of inequalities:

$$c_{m,h} \sum_{h \in \mathcal{H}} (x_{m,h} + y_{m,h})^2 \leq \psi^2_{m,h} \tag{B.2}$$

$$c_{m,h} \sum_{h \in \mathcal{H}} (x_{m,h} + y_{m,h})^2 \geq \psi^2_{m,h} \tag{B.3}$$

$$c_{m,h} \sum_{h \in \mathcal{H}} (x_{m,h} - y_{m,h})^2 \leq \psi^2_{m,h} \tag{B.4}$$

$$c_{m,h} \sum_{h \in \mathcal{H}} (x_{m,h} - y_{m,h})^2 \geq \psi^2_{m,h} \tag{B.5}$$

where we can observe that (B.2) and (B.4) are two convex SOC constraints, while the rest two are still concave. Therefore, we use 1st-order Taylor expansion to linearize them near reference points (denote the left-hand side of (B.3) and (B.5) as $f_{m,h}$ for conciseness):

$$f_{m,h} = f^*_{m,h} + \nabla f_{m,h}|_{f_{m,h}=f^*_{m,h}} (f_{m,h} - f^*_{m,h}) + \delta_{m,h} \geq \psi^2_{m,h} \tag{B.6}$$

where the Taylor remainder $\delta_{m,h}$ will be driven to zero during the sequential programming. Then, these constraints will be equivalent to the original inequalities (B.3) and (B.5).

It is worth-noting that the original bilinearities (42) can also be reformulated into a more general form $c_{m,h} \sum_{h \in \mathcal{H}} (\kappa x_{m,h} + (\kappa)^{-1} y_{m,h})^2 = c_{m,h} \sum_{h \in \mathcal{H}} (\kappa x_{m,h} - (\kappa)^{-1} y_{m,h})^2$. Then, the coefficient κ should be chosen appropriately according to the magnitude of $x_{m,h}$ and $y_{m,h}$ to avoid numerical issues in the solver.

Appendix C. Specific formulations of SOC constraints of gas flow dynamics

When applying the general SOC reformulations in the Appendix B to specific constraints, i.e., motion and advective transport equations, they will be reformulated into the following:

For motion equations when $\gamma_{ij} = 1$:

$$\left\| \begin{matrix} \Delta x^{-\frac{1}{2}} (\overline{\rho}_{ij,s,k} + \Delta p^x_{ij,s,k}), \\ (\frac{\rho_0}{A_{ij}\Delta t})^{\frac{1}{2}} (\overline{\rho}_{ij,s,k} + \Delta Q^t_{ij,s,k}), \\ 2\Theta_{ij} \overline{Q}_{ij,s,k} \end{matrix} \right\| \leq \psi^{mo}_{ij,s,k} \tag{C.1}$$

$$\left\| \begin{matrix} \Delta x^{-\frac{1}{2}} (\overline{\rho}_{ij,s,k} - \Delta p^x_{ij,s,k}), \\ (\frac{\rho_0}{A_{ij}\Delta t})^{\frac{1}{2}} (\overline{\rho}_{ij,s,k} - \Delta Q^t_{ij,s,k}) \end{matrix} \right\| \leq \psi^{mo}_{ij,s,k} \tag{C.2}$$

$$(\psi^{mo}_{ij,s,k})^2 \leq \Delta x^{-1} \left((\overline{\rho}^*_{ij,s,k} + \Delta p^{x*}_{ij,s,k})^2 + 2(\overline{\rho}^*_{ij,s,k} + \Delta p^{x*}_{ij,s,k})(\overline{\rho}_{ij,s,k} - \overline{\rho}^*_{ij,s,k}) \right.$$
$$+ \Delta p^x_{ij,s,k} - \Delta p^{x*}_{ij,s,k}) \bigg) + (\frac{\rho_0}{A_{ij}\Delta t})^{-1} \left((\overline{\rho}^*_{ij,s,k} + \Delta Q^{t*}_{ij,s,k})^2 + 2(\overline{\rho}^*_{ij,s,k} + \Delta Q^{t*}_{ij,s,k}) \right.$$
$$(\overline{\rho}_{ij,s,k} - \overline{\rho}^*_{ij,s,k} + \Delta Q^t_{ij,s,k} - \Delta Q^{t,*}_{ij,s,k}) \bigg) + 4\Theta^2_{ij} \left((\overline{Q}^*_{ij,s,k})^2 + 2\overline{Q}^*_{ij,s,k} \right.$$
$$(\overline{Q}_{ij,s,k} - \overline{Q}^*_{ij,s,k}) \bigg) + \delta^{mo}_{ij,s,k} \tag{C.3}$$

$$(\psi^{mo}_{ij,s,k})^2 \leq \Delta x^{-1} \left((\overline{\rho}^*_{ij,s,k} - \Delta p^{x*}_{ij,s,k})^2 + 2(\overline{\rho}^*_{ij,s,k} - \Delta p^{x*}_{ij,s,k})(\overline{\rho}_{ij,s,k} - \overline{\rho}^*_{ij,s,k}) \right.$$
$$- \Delta p^x_{ij,s,k} + \Delta p^{x*}_{ij,s,k}) \bigg) + (\frac{\rho_0}{A_{ij}\Delta t})^{-1} \left((\overline{\rho}^*_{ij,s,k} - \Delta Q^{t*}_{ij,s,k})^2 + 2(\overline{\rho}^*_{ij,s,k} - \Delta Q^{t*}_{ij,s,k}) \right.$$

$$(\overline{\rho}_{ij,s,k} - \overline{\rho}^*_{ij,s,k} - \Delta Q^t_{ij,s,k} + \Delta Q^{t,*}_{ij,s,k}) \bigg) + \delta^{mo}_{ij,s,k} \tag{C.4}$$

Above is the pair of SOC constraints for motion equations when $\gamma_{ij} = 1$. If $\gamma_{ij} = -1$, similar SOC constraints can also be derived.

For advective transport equations:

$$\left\| \begin{matrix} (\rho_0 \Delta t)^{-\frac{1}{2}} (\Delta \phi^t_{ij,s,k,n} + \overline{\rho}_{ij,s,k}), \\ (A_{ij} \Delta x)^{-\frac{1}{2}} (\Delta \phi^x_{ij,s,k,n} + \overline{Q}_{ij,s,k,n}) \end{matrix} \right\| \leq \psi^{at}_{ij,s,k} \tag{C.5}$$

$$\left\| \begin{matrix} (\rho_0 \Delta t)^{-\frac{1}{2}} (\Delta \phi^t_{ij,s,k,n} - \overline{\rho}_{ij,s,k}), \\ (A_{ij} \Delta x)^{-\frac{1}{2}} (\Delta \phi^x_{ij,s,k,n} - \overline{Q}_{ij,s,k}) \end{matrix} \right\| \leq \psi^{at}_{ij,s,k,n} \tag{C.6}$$

$$(\psi^{at}_{ij,s,k,n})^2 \leq A_{ij} \Delta x \left((\Delta \phi^{t*}_{ij,s,k,n} + \overline{\rho}^*_{ij,s,k})^2 + 2(\phi^{t*}_{ij,s,k,n} + \overline{\rho}^*_{ij,s,k}) \right.$$
$$\times (\phi^t_{ij,s,k,n} - \phi^{t*}_{ij,s,k,n}$$
$$+ \overline{\rho}_{ij,s,k} - \overline{\rho}^*_{ij,s,k}) \bigg) + \Delta t \rho_0 \left((\Delta \phi^{x*}_{ij,s,k,n} + \overline{Q}^*_{ij,s,k})^2 + 2(\phi^{x*}_{ij,s,k,n} + \overline{Q}^*_{ij,s,k}) \right.$$
$$(\phi^x_{ij,s,k,n} - \phi^{x*}_{ij,s,k,n} + \overline{Q}_{ij,s,k} - \overline{Q}^*_{ij,s,k}) \bigg) + \delta^{at}_{ij,s,k,n} \tag{C.7}$$

$$(\psi^{at}_{ij,s,k,n})^2 \leq A_{ij} \Delta x \left((\Delta \phi^{t*}_{ij,s,k,n} - \overline{\rho}^*_{ij,s,k})^2 + 2(\phi^{t*}_{ij,s,k,n} - \overline{\rho}^*_{ij,s,k}) \right.$$
$$\times (\phi^t_{ij,s,k,n} - \phi^{t*}_{ij,s,k,n}$$
$$- \overline{\rho}_{ij,s,k} + \overline{\rho}^*_{ij,s,k}) \bigg) + \Delta t \rho_0 \left((\Delta \phi^{x*}_{ij,s,k,n} - \overline{Q}^*_{ij,s,k})^2 + 2(\phi^{x*}_{ij,s,k,n} - \overline{Q}^*_{ij,s,k}) \right.$$
$$(\phi^x_{ij,s,k,n} - \phi^{x*}_{ij,s,k,n} - \overline{Q}_{ij,s,k} + \overline{Q}^*_{ij,s,k}) \bigg) + \delta^{at}_{ij,s,k,n} \tag{C.8}$$

$$\delta^{mo}_{ij,s,k}, \quad \delta^{at}_{ij,s,k,n} \geq 0 \tag{C.9}$$

where $\delta^{mo}_{ij,s,k}$ and $\delta^{at}_{ij,s,k,n}$ are the slack variables for the Taylor remainders of motion and the advective transport equations, respectively.

References

[1] Li H, Ren Z, Trivedi A, Srinivasan D, Liu P. Optimal planning of dual-zero microgrid on an island towards net-zero carbon emission. IEEE Trans Smart Grid 2023.

[2] Yang S, Lao K-W, Hui H, Chen Y. Secure distributed control for demand response in power systems against deception cyber-attacks with arbitrary patterns. IEEE Trans Power Syst 2024.

[3] HyDeploy project – Project close down report. 2023, [Online]. Available: https://hydeploy.co.uk/app/uploads/2022/06/HyDeploy-Close-Down-Report_Final.pdf.

[4] Launch of Hebei's first demonstration project on natural gas with hydrogen blending. 2023, [Online]. Available: https://news.bjx.com.cn/html/20200917/1105156.shtml.

[5] Yang L, Li H, Zhang H, Wu Q, Cao X. Stochastic-distributionally robust frequency-constrained optimal planning for an isolated microgrid. IEEE Trans Sustain Energy 2024.

[6] Briggs T. The combustion and interchangeability of natural gas on domestic burners. Combustion 2014;4(3).

[7] Haeseldonckx D, D'haeseleer W. The use of the natural-gas pipeline infrastructure for hydrogen transport in a changing market structure. Int J Hydrog Energy 2007;32(10–11):1381–6.

[8] Abeysekera M, Wu J, Jenkins N, Rees M. Steady state analysis of gas networks with distributed injection of alternative gas. Appl Energy 2016;164:991–1002.

[9] Cavana M, Mazza A, Chicco G, Leone P. Electrical and gas networks coupling through hydrogen blending under increasing distributed photovoltaic generation. Appl Energy 2021;290:116764.

[10] Zhang S, Wang S, Zhang Z, Lyu J, Cheng H, Huang M, Zhang Q. Probabilistic multi-energy flow calculation of electricity–gas integrated energy systems with hydrogen injection. IEEE Trans Ind Appl 2022;58(2):2740–50. http://dx.doi.org/10.1109/TIA.2021.3094487.

[11] Cheli L, Guzzo G, Adolfo D, Carcasci C. Steady-state analysis of a natural gas distribution network with hydrogen injection to absorb excess renewable electricity. Int J Hydrog Energy 2021;46(50):25562–77.

[12] Zhou D, Yan S, Huang D, Shao T, Xiao W, Hao J, Wang C, Yu T. Modeling and simulation of the hydrogen blended gas-electricity integrated energy system and influence analysis of hydrogen blending modes. Energy 2022;239:121629. http://dx.doi.org/10.1016/j.energy.2021.121629.

[13] Wu T, Wang J. Reliability evaluation for integrated electricity-gas systems considering hydrogen. IEEE Trans Sustain Energy 2022;14(2):920–34.

[14] Saedi I, Mhanna S, Mancarella P. Integrated electricity and gas system modelling with hydrogen injections and gas composition tracking. Appl Energy 2021;303:117598.

[15] Zhao P, Gu C, Hu Z, Xie D, Hernando-Gil I, Shen Y. Distributionally robust hydrogen optimization with ensured security and multi-energy couplings. IEEE Trans Power Syst 2020;36(1):504–13.

[16] Wang S, Zhai J, Hui H. Optimal energy flow in integrated electricity and gas systems with injection of alternative gas. IEEE Trans Sustain Energy 2023.

[17] Shin J, Werner Y, Kazempour J. Modeling gas flow directions as state variables: Does it provide more flexibility to power systems? Electr Power Syst Res 2022;212:108502.

[18] Raheli E, Werner Y, Kazempour J. Flexibility of integrated power and gas systems: Modeling and solution choices matter. 2023, arXiv preprint arXiv: 2311.05744.

[19] Mhanna S, Saedi I, Mancarella P. Iterative LP-based methods for the multiperiod optimal electricity and gas flow problem. IEEE Trans Power Syst 2021;37(1):153–66.

[20] Raheli E, Wu Q, Zhang M, Wen C. Optimal coordinated operation of integrated natural gas and electric power systems: A review of modeling and solution methods. Renew Sustain Energy Rev 2021;145:111134.

[21] Jiang Y, Ren Z, Dong ZY, Sun Z, Terzija V. An optimal dispatch method of integrated electricity and gas systems incorporating hydrogen injection flexibility. Int J Electr Power Energy Syst 2024;155:109662.

[22] Wang S, Hui H, Zhai J. Short-term reliability assessment of integrated power-gas systems with hydrogen injections using universal generating function. IEEE Trans Ind Appl 2023.

[23] Wang S, Hui H, Ding Y, Song Y. Long-term reliability evaluation of integrated electricity and gas systems considering distributed hydrogen injections. Appl Energy 2024;356:122374.

[24] Wang S, Hui H, Siano P. Resilience of gas interchangeability in hydrogen-blended integrated electricity and gas systems: A transient approach with dynamic gas composition tracking. iEnergy 2023;2(2):143–54.

[25] Yang J, Zhang N, Kang C, Xia Q. Effect of natural gas flow dynamics in robust generation scheduling under wind uncertainty. IEEE Trans Power Syst 2017;33(2):2087–97.

[26] Wang S, Zhai J, Hui H, Ding Y, Song Y. Operational reliability of integrated energy systems considering gas flow dynamics and demand-side flexibilities. IEEE Trans Ind Inf 2023.

[27] Zang H, Geng M, Huang M, Wei Z, Chen S, Sun G. Asynchronous and adaptive state estimation of integrated electricity–gas energy systems. IEEE Internet Things J 2022;10(9):7636–44.

[28] Malley CO, Kourounis D, Hug G, Schenk O. Finite volume methods for transient modeling of gas pipelines. In: 2018 IEEE international energy conference. ENERGYCON, IEEE; 2018, p. 1–6.

[29] Kazi SR, Misra S, Tokareva S, Sundar K, Zlotnik A. Stochastic finite volume method for uncertainty management in gas pipeline network flows. 2024, arXiv preprint arXiv:2403.18124.

[30] Chen B, Guo Q, Yin G, Wang B, Pan Z, Chen Y, Wu W, Sun H. Energy-circuit-based integrated energy management system: theory, implementation, and application. Proc IEEE 2022;110(12):1897–926.

[31] Yang J, Zhang N, Botterud A, Kang C. Situation awareness of electricity-gas coupled systems with a multi-port equivalent gas network model. Appl Energy 2020;258:114029.

[32] Zhou D, Wang C, Yan S, Yan Y, Guo Y, Shao T, Li T, Jia X, Hao J. Dynamic modeling and characteristic analysis of natural gas network with hydrogen injections. Int J Hydrog Energy 2022;47(78):33209–23.

[33] Zhang Z, Saedi I, Mhanna S, Wu K, Mancarella P. Modelling of gas network transient flows with multiple hydrogen injections and gas composition tracking. Int J Hydrog Energy 2022;47(4):2220–33.

[34] Zhou D, Jia X, Peng Z, Ma Y. Coordinate control law analysis for hydrogen blended electricity-gas integrated energy system. Int J Hydrog Energy 2022;47(69):29648–60.

[35] Mhanna S, Saedi I, Mancarella P, Zhang Z. Coordinated operation of electricity and gas-hydrogen systems with transient gas flow and hydrogen concentration tracking. Electr Power Syst Res 2022;211:108499.

[36] Gas safety (management) regulations. 2023, [Online]. Available: https://www.legislation.gov.uk/uksi/1996/551/introduction/made.

[37] Park C, Oh S, Kim C, Choi Y, Ha Y. Effect of natural gas composition and gas interchangeability on performance and emission characteristics in an air–fuel controlled natural gas engine. Fuel 2021;287:119501.

[38] Bus M. Review of the impact of hydrogen addition to natural gas on gas turbine combustion. 2013, URL http://essay.utwente.nl/69334/.

[39] Gersen S, van Essen M, GL D, Teerling O, Heating B. Demonstration of high performance (Low NOx) domestic hydrogen boilers. Res Gate 2020.

[40] Weaver ER. Formulas and graphs for representing the interchangeability of fuel gases. J Res Natl Bur Stand 1951;46(3):214–45.

[41] Osiadacz A. Simulation of transient gas flows in networks. Internat J Numer Methods Fluids 1984;4(1):13–24. http://dx.doi.org/10.1002/fld.1650040103, arXiv:https://onlinelibrary.wiley.com/doi/pdf/10.1002/fld.1650040103.

[42] Ryan MJ, Mailloux RL. Methods for performing composition tracking for pipeline networks. In: PSIG annual meeting. OnePetro; 1986, p. 1.

[43] Menon ES. Gas pipeline hydraulics. Crc Press; 2005.

[44] Zlotnik A, Roald L, Backhaus S, Chertkov M, Andersson G. Coordinated scheduling for interdependent electric power and natural gas infrastructures. IEEE Trans Power Syst 2017;32(1):600–10. http://dx.doi.org/10.1109/TPWRS.2016.2545522.

[45] Overbye TJ, Cheng X, Sun Y. A comparison of the AC and DC power flow models for LMP calculations. In: 37th annual hawaii international conference on system sciences, 2004. proceedings of the. IEEE; 2004, p. 9–pp.

[46] Large-scale security-constrained optimal power flow (SCOPF). 2017, URL https://arpa-e.energy.gov/sites/default/files/E_GD_Speaker2_Lin_PJM.pdf.

[47] Su J, Zhang H, Wong C-K, Yu L, Tan Z. Hierarchical control of inverter air conditioners for frequency regulation service of islanded microgrids with fair power participation. IEEE Trans Smart Grid 2024.

[48] He Y, Yan M, Shahidehpour M, Li Z, Guo C, Wu L, Ding Y. Decentralized optimization of multi-area electricity-natural gas flows based on cone reformulation. IEEE Trans Power Syst 2018;33(4):4531–42. http://dx.doi.org/10.1109/TPWRS.2017.2788052.

[49] Grigg C, Wong P, Albrecht P, Allan R, Bhavaraju M, Billinton R, Chen Q, Fong C, Haddad S, Kuruganty S, et al. The IEEE reliability test system-1996. A report prepared by the reliability test system task force of the application of probability methods subcommittee. IEEE Trans Power Syst 1999;14(3):1010–20.

[50] De Wolf D, Smeers Y. The gas transmission problem solved by an extension of the simplex algorithm. Manage Sci 2000;46(11):1454–65.

[51] Github repository. 2024, [Online]. Available: https://github.com/ShengWang-EE/J11_OEF_gas_composition_dynamics_hydrogen.

[52] What's new in gurobi 11.0. 2023, [Online]. Available: https://cdn.gurobi.com/wp-content/uploads/Whats-New-in-Gurobi-11.0_Webinar-slides.pdf?x34984.

[53] National oceanic and atmospheric administration. 2023, [Online]. Available: https://www.noaa.gov/.

[54] Gas safety (management) regulations 1996. 1996, [Online]. Available: https://www.legislation.gov.uk/uksi/1996/551/introduction/made.

[55] The gas safety (management) (amendment) regulations 2023. 2023, [Online]. Available: https://www.legislation.gov.uk/uksi/2023/284/made.

[56] Natural gas — Quality designation. 2013, [Online]. Available: https://www.iso.org/standard/53058.html.